Science of the Total Environment 648 (2019) 206–217

Contents lists available at ScienceDirect

Science of the Total Environment

journal homepage: www.elsevier.com/locate/scitotenv

Research on the sustainable efficacy of g-MoS_2 decorated biochar nanocomposites for removing tetracycline hydrochloride from antibiotic-polluted aqueous solution

Zhuotong Zeng [a,1], Shujing Ye [b,1], Haipeng Wu [a,b,c,1], Rong Xiao [a,*], Guangming Zeng [a,b,**], Jie Liang [b], Chang Zhang [b], Jiangfang Yu [b], Yilong Fang [b], Biao Song [b]

[a] Department of Dermatology, Second Xiangya Hospital, Central South University, Changsha 410011, PR China
[b] College of Environmental Science and Engineering, Hunan University, Key Laboratory of Environmental Biology and Pollution Control (Hunan University), Ministry of Education, Changsha 410082, PR China
[c] Changjiang River Scientific Research Institute, Wuhan 430010, PR China

HIGHLIGHTS

- Hierarchical g-MoS_2 nanosheets were successfully loaded onto the surface of biochar.
- Pore structures and surface properties of biochar were improved by decorated with g-MoS_2.
- Sustainable efficient removal for TC by novel g-MoS_2-biochar nanocomposite was confirmed.
- Several mechanisms participated in the antibiotic removal were also discussed.
- Further research focuses on the catalytic degradation ability of nanocomposite for its regeneration.

GRAPHICAL ABSTRACT

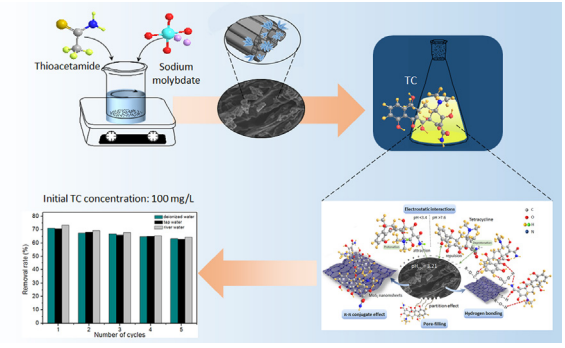

ARTICLE INFO

Article history:
Received 10 May 2018
Received in revised form 27 July 2018
Accepted 7 August 2018
Available online 09 August 2018

Editor: Ching-Hua Huang

Keywords:
Biochar-based nanocomposite
g-MoS_2
Tetracycline hydrochloride

ABSTRACT

Antibiotic concentrations in surface waters far exceed the pollution limit due to the abuse of pharmaceuticals, resulting in an urgent need for an approach with potential efficiency, sustainability and eco-friendliness to remove antibiotic pollutants. A novel biochar-based nanomaterial was synthesized by hydrothermal synthesis and was investigated for its removal potential for tetracycline hydrochloride (TC) from both artificial and real wastewater. The associative facilitation between biochar and g-MoS_2 nanosheets was proposed, revealing the favorable surface structures and adsorption properties of the composite. The related adsorption kinetics, isotherms and thermodynamics were studied by several models with adsorption experimental data, turning out that biochar decorated by g-MoS_2 exhibited optimum TC removal with adsorption capacity up to 249.45 mg/g at 298 K. The adsorption behavior of TC molecules on g-MoS_2-BC can be interpreted well by three-step process, and it is dominated by several mechanisms containing pore-filling, electrostatic force, hydrogen bond and π-π interaction. In addition, the cost-effective g-

* Corresponding author.
** Correspondence to: G. Zeng, College of Environmental Science and Engineering, Hunan University, Key Laboratory of Environmental Biology and Pollution Control (Hunan University), Ministry of Education, Changsha 410082, PR China.
E-mail addresses: xiaorong65@csu.edu.cn (R. Xiao), zgming@hnu.edu.cn (G. Zeng).
[1] These authors contribute equally to this article.

https://doi.org/10.1016/j.scitotenv.2018.08.108
0048-9697/

Sustainable application
Removal mechanisms

MoS_2-BC nanocomposites demonstrated excellent adsorption and recycling performance in TC-contaminated river water, which might provide the underlying insights needed to guide the design of promising approach for contaminant removal on a large scale in practical application.

1. Introduction

Antibiotics, as emerging pollutants, are released into the environment in large quantities due to abuse of pharmaceuticals, and they have been detected excessively in surface water, ground water and sediment (Chao et al., 2014; Zhou et al., 2018). The existence of antibiotic residues in the environment has caused high concern because of their potential long-term adverse threats on human health and natural ecosystem (Ren et al., 2018; Ye et al., 2017b). There is an increasing demand for the removal of antibiotics from contaminated water to avoid the ecological risk. A growing number of researches have been explored for the remediation of antibiotics-contaminated water (Tiwari et al., 2017), containing biotechnology (degrading microorganism) (Chen et al., 2015; Ye et al., 2017a), chemical technology (oxidation, photocatalysis) (Cheng et al., 2016; Wang et al., 2017) and physical technology (separation) (Gong et al., 2009; Wan et al., 2018; Xu et al., 2012b). However, some deficiencies restrict the application of these technologies, for instance, the growth-restricted microorganisms as for biological processes; high energy/cost consumption and toxic byproducts as for chemical processes; and low efficiency as for pure physical separation (Ahmed et al., 2017; Tang et al., 2014). Tetracycline hydrochloride (TC) with amphoteric behavior, a kind of widely used antimicrobial, has been detected frequently in aquatic ecosystems, and it is difficult to degrade even with more toxic byproducts (Homem and Santos, 2011). Adsorption is a way that affects the migration-transformation of antibiotics in the aquatic environment, which is considered as a feasible and economical approach for antibiotic removal (Chao et al., 2017; P.P. Liu et al., 2017; S. Liu et al., 2017).

Adsorbents play an important role in polluted water remediation, some common adsorbents and their modifications have been studied for removal of antibiotics from aqueous solution, such as graphene (Deng et al., 2013; Q.F. Yang et al., 2017), clay minerals (Long et al., 2011; Xu et al., 2012a), metal organic framework (Wang et al., 2018; Yang et al., 2018a, 2018b), carbon nanotubes (Ji et al., 2009; Zhang et al., 2015) and powder activated carbon (P.P. Liu et al., 2017; S. Liu et al., 2017). Among them, biochar shows excellent adsorption performance as well as carbon sequestration based on its favorable physicochemical surface characteristics, like high hydrophobicity and aromaticity, large surface area and developed pore structure (P.P. Liu et al., 2017; S. Liu et al., 2017; Ye et al., 2017a). Moreover, biochar is more environmentally and economically viable, since it is derived from the pyrolysis of waste biomass, allowing the resources recovery and utilization (Liang et al., 2017; Wu et al., 2017; Zeng et al., 2015). However, the effectiveness of biochar relies heavily on the temperatures and raw materials of production. In order to get better removal efficiency for pollutants, biochar is modified by metallic embedding, nanomaterial decorating and surface functionalization based on various mechanisms (Tan et al., 2015; Ye et al., 2017b). Zhang et al. (2012) prepared an engineered graphene-coated biochar, and the results showed the adsorbed amount of contaminant on the graphene-coated biochar was enhanced by the strong π-π interaction between aromatic structure of pollutant molecules and graphene sheets on biochar surface, which was >20 times higher than that of the pristine biochar (Zhang et al., 2012). It is still a challenge to develop a cost-effective adsorbent for water treatment on large scale application, along with the difficulties in separation and regeneration of used adsorbent.

Molybdenum disulfide with a special layered structure (*g*-MoS_2) is a novel quasi-two-dimensional lamellar nanomaterial similar to graphene, which had been proposed as a potential alternative for removal of antibiotics (Chao et al., 2017; Chao et al., 2014; Han et al., 2017; Theerthagiri et al., 2017). A MoS_2 molecule possesses the S-Mo-S sandwich structure with the Mo atom sandwiched between two S atoms. Due to the large surface area, surface covalent forces and strong edge effects (Kiran et al., 2014), the researches of *g*-MoS_2 in contaminant adsorption (Chao et al., 2014; Qiao et al., 2016), electrochemical performance (Voiry et al., 2013; Wang et al., 2016), and catalytic degradation (Vattikuti and Byon, 2016; Zhu et al., 2016), etc. have drawn huge deal of scientific interests. However, *g*-MoS_2 nanosheets have relatively low dispersibility and tend to agglomerate, thereby adversely affecting the remediation efficiency as well as having bad impacts on aquatic organisms. Until now, no systematic study concerning the adsorption performance of MoS_2 nanomaterial-decorated biochar (biochar is used as substrate and is modified to a nanocomposite with *g*-MoS_2 nanosheets) in antibiotic removal from aquatic environment has been published yet.

In this work, a novel adsorbent of *g*-MoS_2 nanosheet-decorated biochar (*g*-MoS_2-BC) was synthesized firstly using a facile hydrothermal method. Batch adsorption experiments were designed to investigate the adsorption performance of the composite in aqueous solution that contaminated with tetracycline hydrochloride (TC). The main aims of the research were to 1) synthesize and characterize the *g*-MoS_2-BC; 2) explore the adsorption behavior of TC on surface of *g*-MoS_2-BC, including the adsorption kinetics, isotherms, thermodynamics, mechanisms as well as the factors potentially affecting the adsorbed amount; and 3) investigate the removal efficiency of *g*-MoS_2-BC applied in real TC wastewater.

2. Materials and methods

2.1. Materials

Rice straw was obtained from bottomland of Dongting Lake, located in Changsha, China. Tetracycline hydrochloride (TC: purity > 98.5%), sodium molybdate and thioacetamide were purchased from Shanghai Chemical Corp and used without purification. Besides, deionized water (18.25 MΩ/cm) used in the experiment was produced by an Ulupure (UPRII-10 T) laboratory water system.

2.2. Preparation of g-MoS_2-decorated biochar

As shown in Fig. 1, biochar was produced by slow pyrolysis of agricultural straw in tube furnace operating at a continuous flow of N_2 gas and a temperature of 500 °C for a residence time of 2 h, according to previous research (Zeng et al., 2015). In a typical synthesis of the MoS_2 nanosheets, 230 mg of $Na_2MoO_4 \cdot 2H_2O$ and 460 mg of thioacetamide were dissolved in 60 mL deionized water, in which 0.1 g of the prepared biochar and 0.1 mM PEG10000 were added in sequence with magnetic stirring, and the mixture dispersed via ultrasonication for 30 min. Afterwards, the whole solution was transferred to a 100 mL Teflon-lined autoclave and heated up to 180 °C for 24 h by hydrothermal treatment. After the mixture was cooled to room temperature naturally, the black solid precipitate (*g*-MoS_2-BC) produced in the solution was collected by centrifugation (8000 rpm for 5 min), and then was washed six times with anhydrous ethanol and deionized water, thereby drying in an oven at 80 °C for overnight.

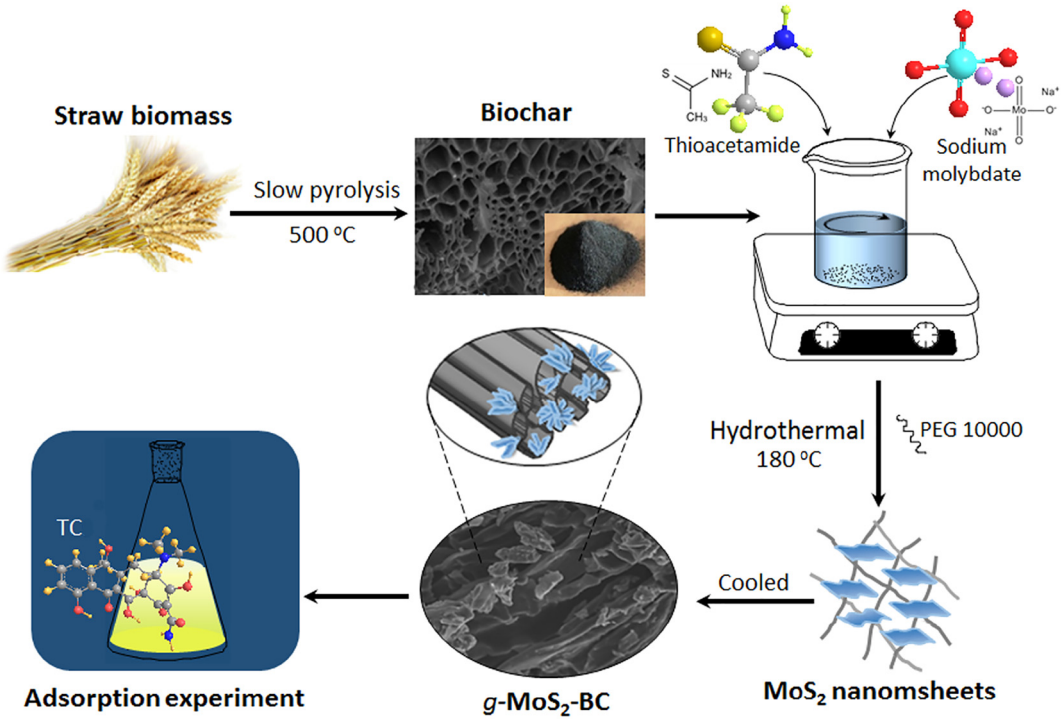

Fig. 1. Schematic illustration of the formation of g-MoS_2-BC composite and its application for removal of TC.

2.3. Characterization methods

The field emission scanning electron microscope (SEM, JSM-6700F, Japan) equipped with an energy dispersive X-ray analyzer (EDS, AMETER, USA) was used to examine the surface morphology and elemental compositions of the g-MoS_2-BC. The structural details of the composite were further characterized by the transmission electron microscopy (TEM). The BET specific surface area and pore characteristics were calculated based on the N_2 adsorption-desorption isotherms at 77.3 K by using automatic surface and porosity analyzer (Quantachrome, USA). Fourier transform infrared spectrum (FT-IR) measurements, recorded in the range of 4000–400 cm^{-1}, were performed in KBr pellet by Nicolet 5700 Spectrometer, USA. The X-ray diffraction (XRD) patterns were showed by Bruker AXS D8 Advance diffractometer equipping with a Cu-K*a* radiation source ($\lambda = 1.5417$ Å) to explore the crystal structures of as-synthesized composite. Binding energies of the material elements were conducted based on the X-ray photoelectron spectroscopy (XPS, Thermo Fisher Scientific-K-Alpha 1063, UK), with the calibration of C1s at 284.8 eV. Thermogravimetric analysis (TGA) was carried out under nitrogen flow with a heating rate of 10 °C/min (TG209, Netzsch, Shanghai, China). The zeta potentials analysis of g-MoS_2-BC and TC were determined using Electroacoustic Spectrometer (ZEN3600 Zetasizer, UK) at solution pH ranging from 2.0 to 11.0.

2.4. Adsorption and removal of TC by g-MoS_2-BC

The batch experiments were carried out in 100 mL Erlenmeyer flasks containing the mixture of 20 mg g-MoS_2-BC and 50 mL TC aqueous solution. All flasks were wrapped with aluminum foils to avoid photodegradation and then placed in a thermostatic water shaking bath at an agitation speed of 150 rpm. The desired pH of solution were achieved by the adjustment with 0.1 M NaOH or 0.1 M HCl measured by pH meter (PHSJ-5, China), varying from 2.0 to 11.0 in initial TC solution (100 mg/L). The effect of salt ionic strength on the removal of TC (100 mg/L) was studied with the sodium chloride (NaCl) and calcium chloride ($CaCl_2$) at concentration range of 0–0.1 M. After shaking under 298 K for 24 h, the samples were taken from the flasks, followed by centrifuged and filtered using 0.45 μm PVDF disposable filters prior to UV spectrophotometry (UV-2550, SHIMADZU, Japan) at λ_{max} 357 nm.

Adsorption kinetics studies were carried out by mixing 20 mg of as-synthesized composite and 50 mL TC solution with initial concentration of 50, 100, 150 mg/L at pH of 4.0. The solution was shaken with a speed of 150 rpm at temperature of 298 K, and samples were taken at predetermined time intervals (from 5 min to 30 h) for the determination of TC residual concentration after filtration. Adsorption isotherm and thermodynamic experiments of g-MoS_2-BC were performed under three different temperatures (298, 308, and 318 K). 50 mL TC solutions with different initial concentrations ranging from 10 to 400 mg/L were adjusted to pH at 4.0 and then mixed with 20 mg composite for shaking. The TC concentrations of sample were then determined by above-mentioned ultraviolet spectrophotometry method after centrifugation and filtration.

The research on practical application of g-MoS_2-BC in real water samples (river water: obtained from Xiang River located in Changsha for TC solution preparation without filtration) was conducted by mixing 20 mg of g-MoS_2-BC with 50 mL real wastewater polluted by TC (100 mg/L), and the mixture was shaken at 298 K for 24 h. The regeneration of g-MoS_2-BC was carried out by adding TC-loaded g-MoS_2-BC to 50 mL NaOH (0.2 mol/L) and stirring the mixture at temperature of 298 K and agitation speed of 140 r/min for 24 h. The suspension liquid was centrifuged after desorption, and the collected solid (regenerated g-MoS_2-BC) was dried at 353 K and applied for next round of adsorption experiment with four-times repetition.

3. Results and discussion

3.1. Characterization of g-MoS_2-BC composite

The surface morphologies and micro-structures of the manufactured materials were examined by SEM and TEM. The SEM image of pristine biochar (Fig. 2a) shows essentially the smooth surface morphology composing of closely packed tubular structures with a cavity size of

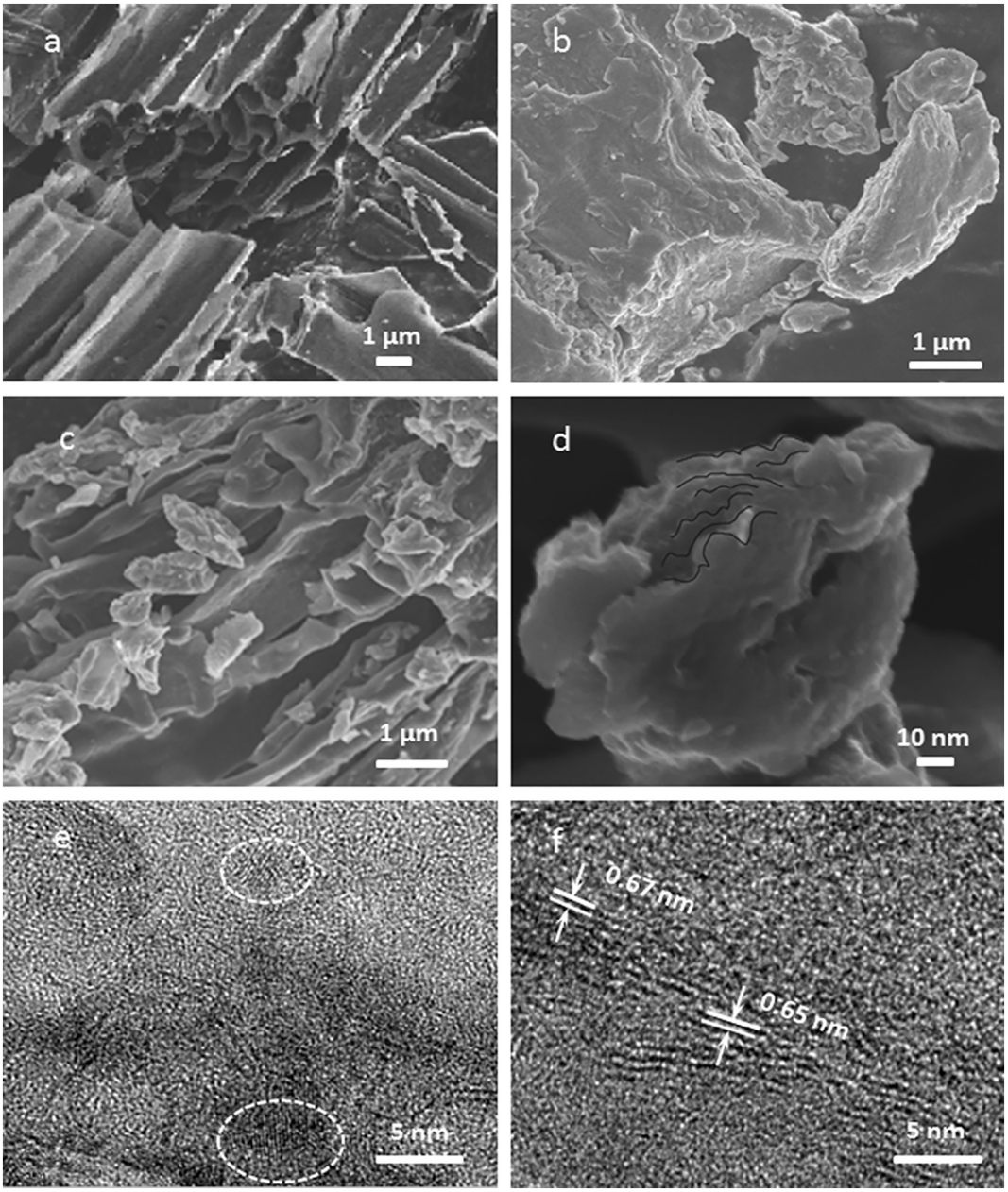

Fig. 2. SEM images of pristine biochar (a), pure MoS_2 (b), *g*-MoS_2-BC (c), and MoS_2 sheets on *g*-MoS_2-BC composite (d), and HRTEM images of *g*-MoS_2-BC (e and f).

1–2 μm. Upon the modification, the resulting *g*-MoS_2-BC composite was found to be relatively uneven surface decorated with MoS_2 stacking hierarchical structure. A high magnification SEM image of the composite, presented in Fig. 2c, reveals that the tubular carbon material is disorderly assembled by crumpled nanosheets with curved edges, indicating the biochar could be regarded as a fresh substrate for supporting hierarchical MoS_2 nanosheets. The interactions between the oxygen-containing functional groups of biochar and Mo^{4+} precursors might be responsible for the in situ growth of MoS_2 nanosheets on biochar surface (Chang and Chen, 2011; Zhao et al., 2017). Compared with the bulk structure of pure MoS_2 (Fig. 2b), the MoS_2 in composite (Fig. 2d) exhibits cluster framework with relatively few layers stacking, which is conducive to the exposure of active sites with defect-rich structure. The TEM images (Fig. S2) and HRTEM (Fig. e and f) further confirm a hierarchical crumpled and disordered structure with curved edges onto the carbon-based materials. HRTEM image illustrates the discontinued fringes of the curled edges, indicating the defect-rich structure with ample surface sites (Qiao et al., 2017). The lattice fringes of *g*-MoS_2 on composite display interplanar spacing of ~0.67 nm, the different interlayer distances should be associated with the intercalation of MoS_2 nanosheets and biochar.

In order to examine the porous properties of *g*-MoS_2-BC composite, Brunauer-Emmett-Teller (BET) gas sorptometry measurement was conducted. The inset of Fig. 3a describes the N_2 adsorption/desorption isotherm of the composite, which can be identified as type IV isotherm with a hysteresis loop, demonstrating the mesoporous characteristic of *g*-MoS_2-BC. The observed large hysteresis loop is intermediate between typical H3- and H4-type isotherm, which is considered to be derived from the stack of laminated layered structure of the slit pore. The corresponding pore-size distribution, obtained from the isotherm by using the BJH method and shown in Fig. 3a, elucidates that most of the pores fall into the size range of 2 to 20 nm and the average pore diameter is calculated to be 3.509 nm. It is well established that adsorbent might exhibit the best adsorption performance when its pore diameter is 1.7–3 times larger than the adsorbate molecular size (even >3–6 times if adsorbent needs to be recycled) (Tang et al., 2018). Taking the

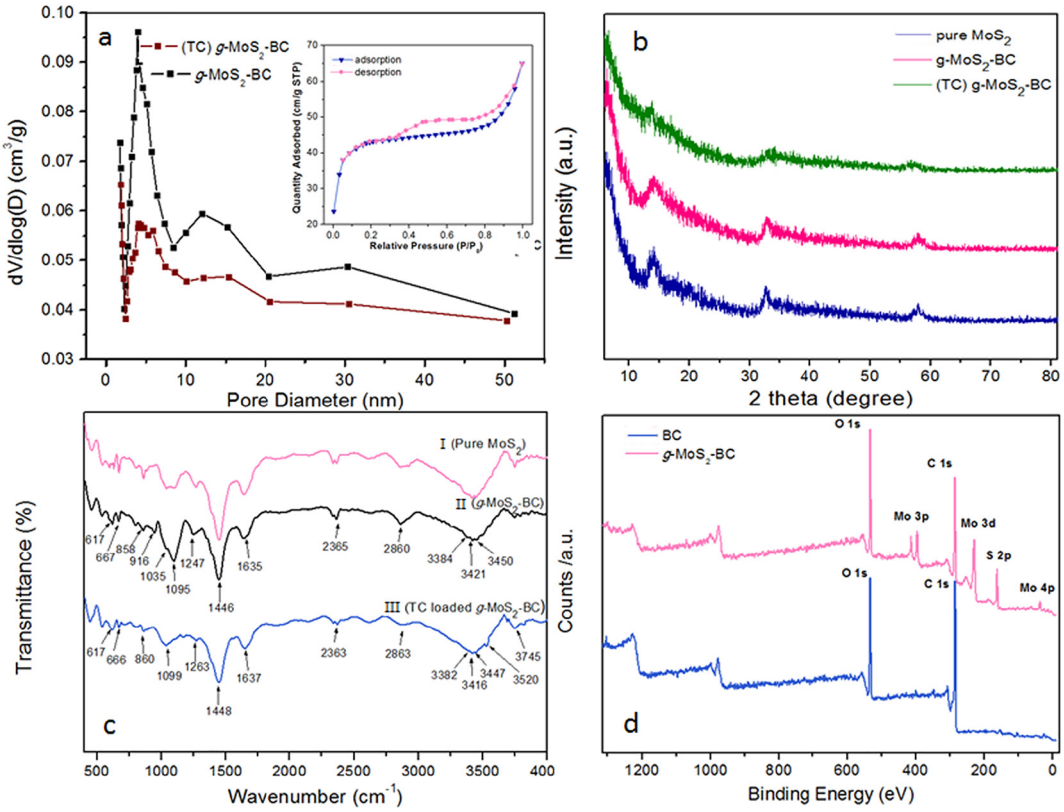

Fig. 3. (a) The pore-size distribution curve of g-MoS_2-BC and TC-loaded g-MoS_2-BC, inset shows N_2 adsorption-desorption isotherms of g-MoS_2-BC at 77 K; (b) XRD patterns of pure MoS_2, g-MoS_2-BC and TC-loaded g-MoS_2-BC; (c) FT-IR spectrums of pure MoS_2, g-MoS_2-BC and TC-loaded g-MoS_2-BC; (d) XPS survey spectra of pristine biochar and g-MoS_2-BC.

TC molecule dimension (1.41 nm long, 0.46 nm wide and 0.82 nm high) into account, we conclude that g-MoS_2-BC composite is endowed with adsorption capacity for efficient TC molecular removal based on their pore-size distribution. On the whole, the prepared composite exhibits a BET specific surface area of 176.8 m^2/g and a pore volume of 0.0839 cm^3/g. Both are higher than the corresponding value of the pristine biochar, it should be noted that the change could be attributed to the extra mosaic structure of MoS_2 nanosheets with plenty of folded edges like wings.

The X-ray powder diffraction (XRD) patterns of the as-prepared MoS_2 and g-MoS_2-BC composite are shown in Fig. 3b. The three detected diffraction peaks are indexed to (002), (100) and (110) planes, respectively, indicating a hexagonal phase of MoS_2 (JCPDS card No. 37-1492) (Chao et al., 2014). Subtle changes in the peak location may be due to the strain effect by bending of the layers or lattice expansion introduced by crystal defects (Berdinsky et al., 2005). Especially, the (002) diffraction peak, resulted primarily from the scattering of interlayer Mo—Mo (L. Yang et al., 2017), is feeble in the pattern, suggesting that MoS_2 is consisted of only a few layers nanosheets. There is no obvious difference in peak position between pure MoS_2 and the g-MoS_2-BC composite due to the low XRD intensity of biochar, which also reveals that the chemical composition of MoS_2 has not changed after the surface modification. From the variation in width and strength of (002) plane diffraction peak, it can be observed that the growth of MoS_2 crystal along the *c*-axis in composite is inhibited owing to the presence of biochar, demonstrating fewer stack of MoS_2 layers.

FT-IR analysis was carried out to investigate the surface property of the BC and g-MoS_2-BC composite. It can be seen from Fig. 3c, several characteristic FT-IR peaks of biochar are observed in composite, including 3384–3450 cm^{-1} for O—H stretching, 2860 cm^{-1} for C—O of carboxyl, 2365 cm^{-1} for cumulated double bonds stretching, 1635 cm^{-1} for C═O vibration, 1446 cm^{-1} for aromatic benzene ring skeletal vibration, 1247 cm^{-1} for C-O stretching, 1039 and 1095 cm^{-1} for C—O—C pyranose ring skeletal vibration, 858 cm^{-1} for C—H bending vibrations and 667 cm^{-1} for S—H vibration. In addition to the common functional groups above mentioned, a new stretch at 617 cm^{-1} appearing in curve (II) is assigned to γ_{as} Mo—S vibration (Wang et al., 2016), demonstrating the successful binding of MoS_2 onto the biochar surface. Moreover, another fresh peak presenting at 916 cm^{-1} in curve (II) could be ascribed to the stretching vibration of Mo═O (Han et al., 2017), which implies the partial oxidation of the Mo atom on edge of nanosheet. Curve (III) in Fig. 3c describes the FT-IR spectrum of TC-loaded g-MoS_2-BC, the enhanced and broadened peaks approximately at 3500 to 3900 cm^{-1} are probably originated from the extra functional groups of TC molecule, especially the peak around 3520 cm^{-1} corresponding to the acylamino of TC. These observations confirmed that the TC molecules are successfully adsorbed on the surface of g-MoS_2-BC composite.

X-ray photoelectron spectroscopy (XPS) was performed to further investigate the surface chemical composition and valence state of the elements in g-MoS_2-BC composite. The survey spectrum, presented in Fig. 3d, reveals the g-MoS_2-BC composite is composed of four major elements of C, O, Mo, and S. Compared with the biochar before and after modification, besides the introduction of Mo, and S elements in g-MoS_2-BC, the proportion of oxygen in the element composition is observed to increase, which implies that more oxygen-containing functional groups appear on composite surface. In the high resolution XPS spectrum of Mo 3d, shown in Fig. 4a, two peaks locating at 232.30 eV and 229.00 eV can be assigned to Mo $3d_{3/2}$ and Mo $3d_{5/2}$, respectively, characterizing of Mo^{4+} in 1 T-MoS_2, while the doublet peaks presenting at about 233.28 and 229.76 eV are attributed to the $3d_{3/2}$ and $3d_{5/2}$ of Mo^{4+} in 2H–MoS_2 (Qiao et al., 2016). Meanwhile, two weak peaks centering at 236.17 and 232.90 eV are attributed to the oxidation state Mo^{6+}, which might be derived from the slight oxidation of Mo atoms at the defect or edges of MoS_2 nanosheets due to the high oxidation activity (Zhou et al., 2014). The peaks at 163.80 and 162.20 eV (Fig. 4b) could be indexed to S 2p1/2 and S 2p3/2 orbital of divalent sulfide,

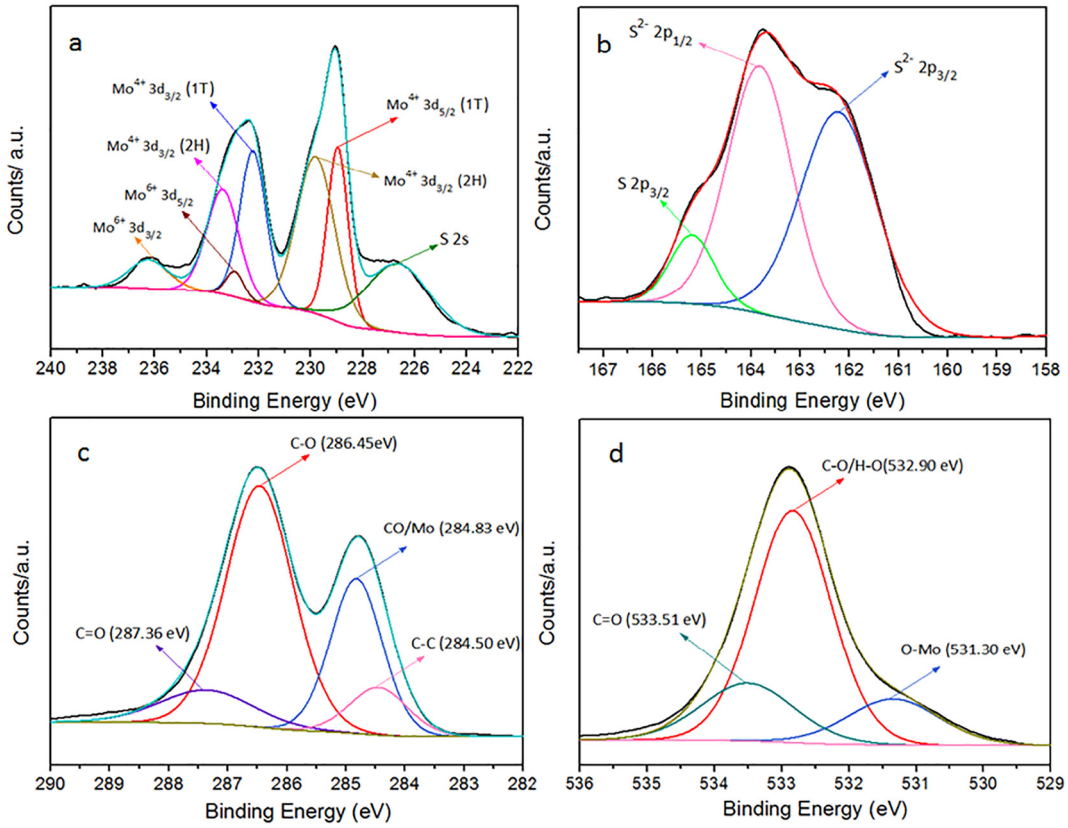

Fig. 4. The XPS spectra of *g*-MoS_2-BC composite: high resolution XPS spectrum of Mo 3d and S 2s (a), S 2p (b), C 1s (c), and O 1s (d).

respectively, suggesting the valence state of S element is −2. In combination with another analysis of peak at 226.66 eV (Fig. 4a) arising from S 2 s, the existence of MoS_2 on the composite is confirmed. In the C 1s XPS spectrum (Fig. 4c) of composite, the C 1s band is deconvoluted into four peaks locating at 284.50, 284.83, 286.45, and 287.36 eV, assigning to the binding of C═C/C—C, CO/Mo, C—O and C═O, respectively. The binding energies of O 1s peaks (Fig. 4d) are observed at about 532.90, 531.30 and 533.51 eV, corresponding to the O—C/O—H, O—Mo and O═C, respectively, which are consistent with the FT-IR results.

The thermal stability of the prepared materials was examined by TGA which is shown in Fig. S3. The weight percentage of both materials was observed to decrease with increasing temperature from 20 to 800 °C. Compared with the pristine biochar, modified biochar has considerably high thermal stability before 450 °C with an approximate 5% weight loss. However, the weight percentage of *g*-MoS_2-BC dropped sharply after 500 °C, which could be attributed to the decomposition of the loaded MoS_2 and organic species that adsorbed on material surface during synthesis process.

3.2. Effect of pH on TC adsorption

It is generally believed that pH plays an important role in influencing adsorption capacity by changing both surface properties of adsorbent and adsorbate. The effect of solution pH varying from 2.0 to 11.0 on TC adsorption to *g*-MoS_2-BC was investigated, and the corresponding results with the zeta potential of *g*-MoS_2-BC are measured and illustrated in Fig. 5a. It could be observed that the adsorption capacity exhibits increasing trend when pH value changes from 2.0 to 4.0, but the effect is little when pH value in the range of 5.0–7.0, sequentially, the declining trend of adsorption capacity is obvious especially when pH value >8.0.

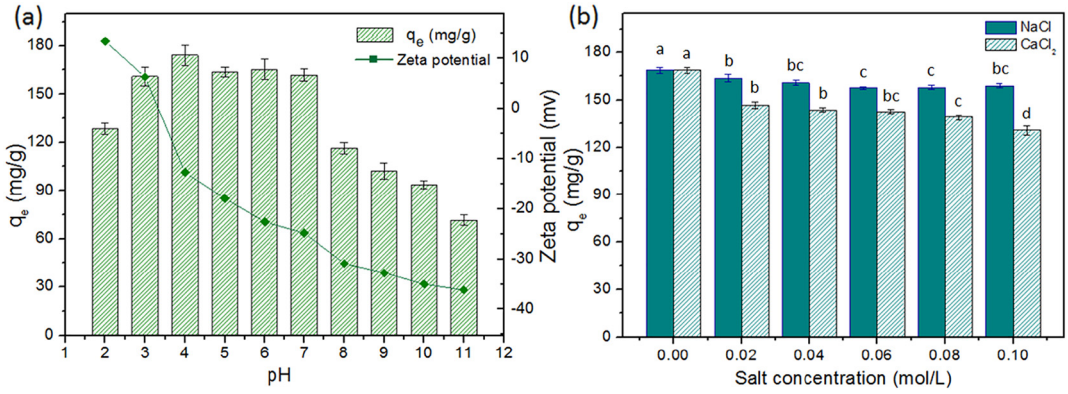

Fig. 5. (a) Zeta potentials of *g*-MoS_2-BC at different pH ranging from 2.0–11.0 and the effect of pH values, (b) effect of ionic strength on adsorption capacity of *g*-MoS_2-BC for TC. Error bars represent standard error of the mean (n = 3). Different letters indicate significant difference ($p < 0.05$) between each salt concentration.

The surface charge of g-MoS_2-BC, which makes great influences on the adsorption process of TC, is sensitive to the solution pH value. According to the result obtained by Fig. 5a, the zero potential point (pH_{ZPC}) of g-MoS_2-BC is around 3.21, the adsorbent surface shows electronegative and decreases gradually with increasing pH value when pH > pH_{ZPC}, owing to the dissociation of carboxylic group on the surface of g-MoS_2-BC. Besides the charge change of adsorbent surface, the chemical speciation of organic compound also transforms by the protonation-deprotonation transition of functional groups at different pH (Tan et al., 2016a). Tetracycline is amphoteric molecule along with multiple ionizable functional groups, which exists cations (TCH_3^+: derived from protonation of the dimethyl-ammonium group), zwitterions (TCH_2^0: derived from deprotonation of the phenolic diketone moiety), and anions (TCH^- and TC^{2-}: derived from deprotonation of the tri-carbonyl groups and phenolic diketone moiety) in accordance with the different dissociation constant (pK_a = 3.4, 7.6 and 9.7) (Chao et al., 2017). When the pH value is below 3.21, both surface zeta potential of TC and g-MoS_2-BC composite are positive and decrease with the increasing pH value of the solution, demonstrating the weakening effect of the electrostatic repulsion which is favorable for adsorption. TC is predominantly existed as zwitterion at pH values ranging of 4.0–7.0 with almost no net electrical charge, resulting in little electrostatic interactions (attraction or repulsion) and unobvious effect of pH changing on the adsorption capacity. The comparatively large adsorption capacity at pH in this range may be determined by other interactions, such as hydrogen bond, π-π and hydrophobic interaction (Chao et al., 2017), as will be described below. Nevertheless, when pH value is >8, the negatively charged surface of g-MoS_2-BC is generally decreases and presents an enhancing electrostatic repulsion to anions TCH^- and TC^{2-}, which adversely affects the adsorbed amount of TC.

3.3. Effect of ionic strength on the adsorption capacity

In order to get closer to the actual situation of natural water, different amounts of sodium chloride and calcium chloride ranging from 0 to 0.1 mol/L were added to solution to explore the influences of ionic strength on the adsorption capacity. As can be seen from Fig. 5b, the addition of extra ions slightly decreases the adsorbed amount of TC in generally, while the adsorption capacity changes very little with the increasing NaCl concentration. There are two possible reasons accounted for the slight change: (1) equalizing effect: on one hand, the Na^+ ions inhibit the electrostatic interaction between the TC cations with g-MoS_2-BC groups by competition (Wu et al., 2014); on the other hand, the salt would be beneficial for the dissociation of TC molecules to TC^+ by facilitating the protonation and result in promoting electrostatic interaction (Tan et al., 2016b). And (2) electrostatic interaction is only a considerably weak mechanism that affects the adsorption of TC on g-MoS_2-BC. However, the downtrend is evident and it represents obvious inhibiting effect of TC adsorption with the increase of $CaCl_2$ concentration. This difference may arise from much higher screening effect by $CaCl_2$ on the electrostatic interaction compared with NaCl, and thus more actives sites are occupied by Ca^{2+}, which confirms the electrostatic interaction has a certain degree in the domination of adsorption.

3.4. Effect of time and adsorption kinetics

As shown in Fig. 6a, the adsorption of TC by g-MoS_2-BC is a time-dependent process, which could be divided into two phases: fast- and slow- adsorption stages. Attributed to the abundant active sites and attractive electrostatic force on composite surface for TC molecules, it is found that the adsorbed amount increased as the increasing contact time, and nearly 85% of the adsorption capacity was accomplished within the first 4 h, which is defined as fast-adsorption stages. Then, the adsorption was performed at much lower rate. The adsorption rate went down gradually until there was no significant variation in the adsorbed amount after 24 h, which represents that the adsorption equilibrium has been achieved.

In order to further analyze the kinetics of TC adsorption onto g-MoS_2-BC, the experimental data were fitted by pseudo-first-order, pseudo-second-order, intra-particle diffusion, Boyd's film-diffusion and Bangham channel diffusion models at three different initial TC concentrations to research the characteristics of the adsorption process in this study. The linear forms of these kinetic models are presented in Table S1, and the related kinetic parameters calculated by linear regression are summarized in Tables 1 and 2.

The pseudo-first-order and pseudo-second-order models are two universal model widely used for investigation of the adsorption kinetics. Compared with the pseudo-first-order model, pseudo-second-order model is more consistent with the adsorption behavior across the whole experimental on the basis of the significant higher values of correlation coefficient (Table 1). This is also supported by the favorable fitting between the equilibrium adsorption capacity obtained from experimental data ($q_{e,\exp}$) and the calculated values ($q_{e,cal}$) in pseudo-second-order model, suggesting the adsorption behavior is much affected by chemical mechanism. It should also be mentioned that the pseudo-second-order rate constants (k_2) reduces with increasing initial TC concentration, which could be attributed to the low competition of TC molecules for adsorption sites at lower initial concentration.

To achieve a better understanding of the diffusion mechanisms and possible rate controlling adsorption process, Intra-particle diffusion, Boyd's film-diffusion and Bangham channel diffusion model were further applied. Intra-particle diffusion model, an empirically functional relationship of adsorbed amount, is used to analyze experimental data with some crucial parameters (intra-particle diffusion rate constant k_{id}, and C_i related to the thickness of boundary layer). As can be seen from part d of Fig. 6, the plots of q_t against $t^{1/2}$ are consisted of three linear sections, indicating that the TC adsorption processes are associated with multiple steps. High linear correlation coefficient and all non-zero C_i values, presented in Table 2, imply that intra-particle diffusion is involved in the adsorption process, while it is not the only rate-controlling step (Wu et al., 2014). The first linear section with a relatively sharp slope demonstrates the transport of TC from bulk solution to the external surface of g-MoS_2-BC, which is controlled by the molecule diffusion and film diffusion. The second section with slow slope describes the gradual adsorption stage, where the intra-particle diffusion dominates, that is, the diffusion of the TC molecules transfer into the pores of g-MoS_2-BC from its external surface. The last linear section with tardy slope implies the arrival of adsorption equilibrium. Comparing the rate constant of three stages, k_{1d} is much larger than other two values, indicating that the film diffusion of TC molecules transferring through the boundary liquid layer is the most important limiting step of the adsorption. The wing-like g-MoS_2 with a quasi-two-dimensional few-layered structure, embedded in the biochar surface, helps TC molecules reach the active sites of surface more easily, since the TC molecules only need to divert from liquid phase through the boundary liquid membrane, but barely need to transfer in limited intermediate layer (Chao et al., 2017).

To shed light on the actual rate-controlling step participated in the overall TC adsorption process, the Boyd's film-diffusion and Bangham channel diffusion model were used to illustrate the experimental data. On the basis of these models, the linearity of the plots provides the fairly reliable information to define the actual rate-controlling step as film diffusion or intra-particle diffusion. The plots of calculated B_t versus time t for early stage of first 8 h are the segment-line which do not pass through the origin, suggesting that the rate-controlling step is dominated by film diffusion at the initial stage of adsorption process, subsequently took over by other mechanisms (intra-particle diffusion). Furthermore, the relatively good linear coefficients of Bangham channel diffusion model, presented in Table 1, reveal the performance of channel diffusion behavior in this adsorption process. In general, the adsorption of TC onto the surface of g-MoS_2-BC includes three steps: (1) the TC

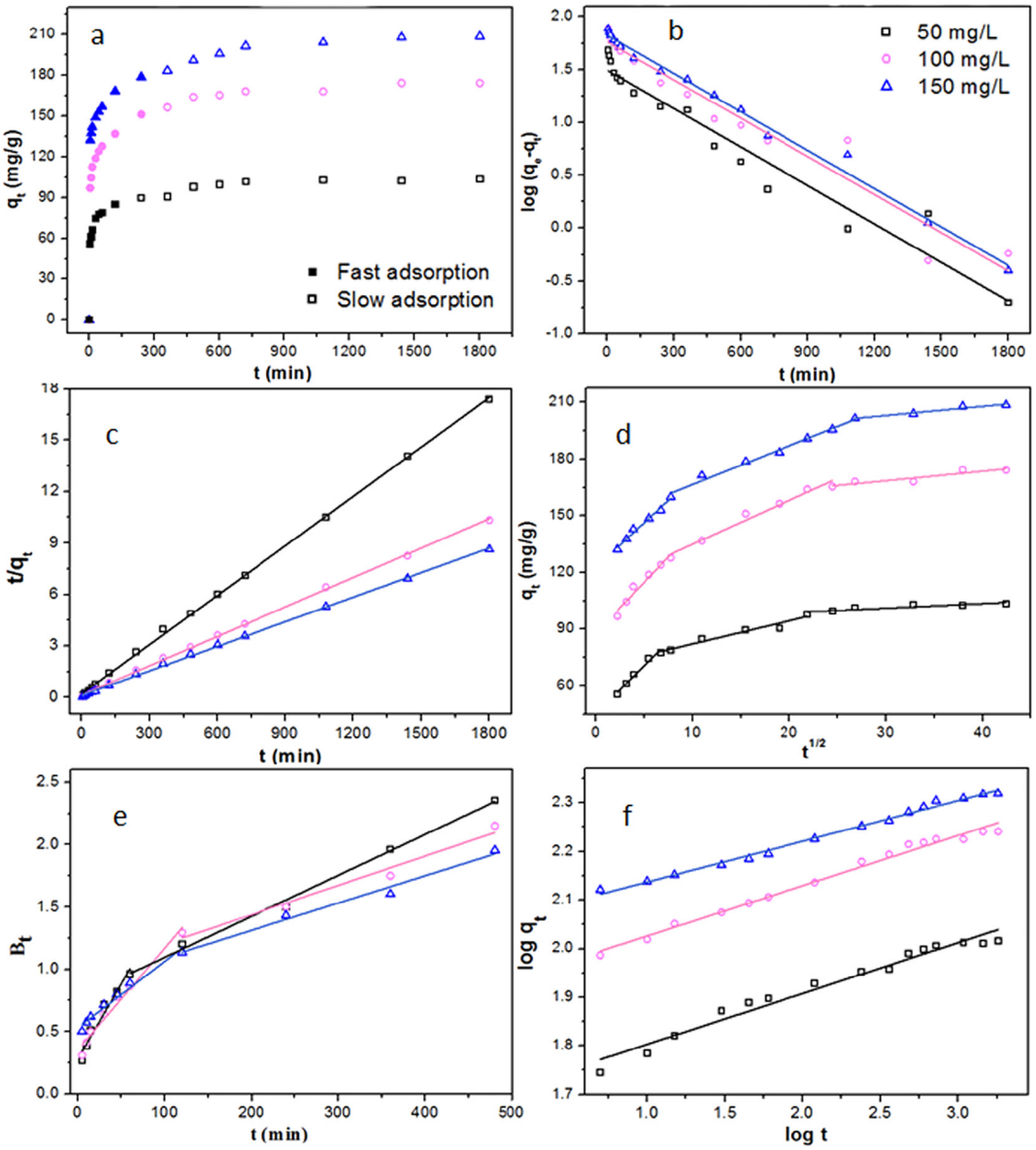

Fig. 6. Effect of contact time on the adsorption of TC onto g-MoS_2-BC (a); the pseudo-first-order plots (b), pseudo-second-order plots (c), intra-particle diffusion plots (d), Boyd plots (e) and Bangham plots (f) for TC adsorption by g-MoS_2-BC.

molecules overcome the liquid resistance and transfer from the solution phase to the exterior surface of g-MoS_2-BC controlled by film diffusion; (2) the TC molecules migrate on the surface and enter the pores of particles, as the adsorbent particles are loaded with TC; and (3) the TC molecules that arrived at the active site are absorbed on the interior surface of g-MoS_2-BC and gradually reach the adsorption equilibrium.

3.5. Adsorption isotherms

The isotherm plays an important role in designing the adsorption system, which shows the distribution of solute molecules in solution phase and solid phase upon adsorption reaching equilibrium. The relationship between the equilibrium adsorption capacity (q_e) and equilibrium TC concentration (C_e) in solution, presented in Fig. S4a, shows the adsorption capacity of g-MoS_2-BC enhances with increasing initial TC concentration in the range of 10–400 mg/L. This may be explained by the more powerful driving force provided by higher initial TC concentration to overcome the mass transfer resistances between aqueous and solid phases (Qiao et al., 2016). To further explore the isotherms, the adsorption equilibrium data at temperature of 298, 308, and 318 K were fitted by different equilibrium models including Langmuir, Freundlich, Temkin, BET isotherm and Dubinin-Redushckevich (D-R)

Table 1
Adsorption kinetics parameters of pseudo-first-order kinetic, pseudo-second-order kinetic and Bangham model for TC on g-MoS_2-BC.

Concentration (mg/L)	Pseudo-first-order kinetic				Pseudo-second-order kinetic			Bangham model		
	$q_{e,exp}$ (mg/g)	k_1 (1/h)	$q_{e,cal}$ (mg/g)	R^2	k_2 (g/mg·h)	$q_{e,cal}$ (mg/g)	R^2	k_B	m	R^2
50	103.676	0.002303	31.225	0.9428	0.000465	104.167	0.9994	49.957	9.560	0.9672
100	174.285	0.002763	58.144	0.9448	0.000248	175.438	0.9993	83.714	9.701	0.9876
150	208.583	0.002994	66.911	0.9807	0.000203	209.643	0.9992	113.083	11.936	0.9927

Table 2
The obtained parameters' value of intra-particle and Boyd's film-diffusion models.

Kinetics models	Parameters		Initial concentration (mg/L)		
			50	100	150
Intra-particle diffusion	K_{id} (mg/g·min$^{1/2}$)	K_{1d}	4.986	5.403	4.738
		K_{2d}	1.225	2.316	2.058
		K_{3d}	0.244	0.516	0.484
	C_i	C_1	45.502	87.822	122.691
		C_2	69.932	111.834	146.113
		C_3	93.766	153.521	188.554
	R_i^2	R_1^2	0.9694	0.9580	0.9831
		R_2^2	0.9524	0.9691	0.9854
		R_3^2	0.8063	0.8691	0.9425
Boyd's film-diffusion	R_i^2	R_1^2	0.9468	0.9724	0.9702
		R_2^2	0.9947	0.9673	0.9771

isotherm models. The forms of these isotherm models and their related isotherm parameters are presented in Tables S1 and 3, respectively.

The Langmuir model, based on the assumption of monolayer adsorption on specific homogenous sites without interactions between molecules, is shown in Fig. S4b. The linear relation is obtained from C_e/q_e against C_e with highest correlation coefficients, revealing that the adsorption of TC onto g-MoS_2-BC probably is monolayer molecular adsorption associated with the functions of chemical mechanism. Concerning the different temperature, the parameters q_{max} and k_L increases as temperature rises up, implying higher temperature is likely to inspire adsorption through enhancing the bond energy between TC molecules and surface sites (Tang et al., 2018). It is noteworthy that a critical characteristic, the dimensionless constant separation factor R_L, is found to be between 0 and 1, which suggests that the adsorption process is favorable. As an improvement of the Langmuir model, the BET adsorption isotherm model is based on the assumption that the adsorbates are randomly adsorbed on a homogeneous surface to form a multi-molecular layer without horizontal interaction. The TC adsorption equilibrium data is fitted better by BET model (inset of Fig. S4b) with higher correlation coefficient (Table 3), demonstrating the adsorption on g-MoS_2-BC surface may be multilayer formation (Jahangiri-Rad et al., 2013).

Freundlich model is an empirical formula which assumes that there are multilayers of adsorbate on heterogeneous surface. It can fit the experimental data well as indicated by the good correlation coefficients ($R^2 > 0.948$), suggesting that the physical interaction also takes part in the TC adsorption on g-MoS_2-BC surface. The K_F value, represented the adsorption capacity, was observed to increase with the increasing temperature. An essential parameter, heterogeneity factor 1 / n, is used to describe the bond distribution, and all 1 / n values are <1, suggesting the adsorption is facile and favorable at all tested temperature. On the whole, the adsorption behavior of TC molecular onto the g-MoS_2-BC surface is determined by the combined impacts of the physical and chemical mechanisms.

In contrast to the models mentioned above, the Temkin isotherm model assumes that the adsorption heat of the adsorbate on the surface decreases linearly with increasing coverage, which is closer to the actual state of the adsorption experiment. As shown in Fig. S4d, the linear regression plot of q_e versus lnC_e is relatively weak observed by the correlation coefficients (R^2) in range of 0.915–0.965, which reveals that the chemical mechanism is not the only controlled interaction for the TC adsorption behavior. This is consistent with the calculated values of b_T (related to the heat of adsorption) in Table 3, since the low b_T value reflects the comparatively weak chemical interaction between TC molecules and surface of g-MoS_2-BC (Wu et al., 2014). Finally, the D-R isotherm model was also analyzed in its linearized form regarding to the TC concentration at equilibrium. The calculated sorption free energy values (E) shown in Table 3 are lower than 8, confirming the occurrence of physical adsorption behavior of TC molecular. However, given the relatively small correlation coefficient, the physical driving force is considered to have a limited role in TC adsorption process.

Table 3
The obtained results of isotherm models for TC adsorption.

Isotherm models	Parameters	Temperature (K)		
		298	308	318
Langmuir	R^2	0.9927	0.9919	0.9913
	K_L (L/mg)	0.0553	0.0637	0.0887
	q_{max} (mg/g)	249.376	423.728	699.301
	R_L	0.0692	0.0803	0.1017
BET model	R^2	0.9981	0.9953	0.9928
	K_b	4430.910	3202.787	2782.223
	q_{max} (mg/g)	248.561	422.386	696.492
Freundlich	R^2	0.9473	0.9745	0.9772
	K_F (L/mg)	30.572	40.988	64.508
	1 / n	0.447	0.497	0.529
Temkin	R^2	0.9651	0.9358	0.9169
	K_T (L/mg)	73.402	136.687	142.263
	B_T	30.154	40.119	51.088
	b_T (J/mol)	82.246	63.889	57.799
D-R model	R^2	0.8138	0.7713	0.7604
	E (kJ/mol)	0.863	0.992	1.107
	q_{max} (mg/g)	168.891	243.464	315.977

3.6. Thermodynamic analysis

As can be seen from part a of Fig. S4, temperature is observed to have a significant effect on TC adsorption behavior. The adsorption capacity improves obviously with the increasing temperature, and the average adsorption capacity increases from 174.701 mg/g at 298 K to 226.653 mg/g at 318 K with about 30% rises under initial TC concentration of 100 mg/L, which suggests that the adsorption is an endothermic process. High temperature is favorable for adsorption, due to the swelling effect on the particle porosity which makes the pore volume allow TC molecules to rapidly diffuse through the external boundary layer and within interior pore of g-MoS_2-BC. The adsorption of TC under different temperature was investigated to make clear the thermodynamic property. Related parameters containing the Gibbs free energy (ΔG^o), enthalpy (ΔH^o), and entropy (ΔS^o) were determined by Gibbs-Helmholtz equation. All negative values of ΔG^o, shown in Table S2, confirm that the absorption process of TC molecules on g-MoS_2-BC surface is spontaneous and feasible, and it is observed to decrease from −4.649 kJ/mol to −9.129 kJ/mol as the temperature increasing, manifesting that the adsorption is more favorable at higher temperature. The ΔG^o value is in the range of −20–0 kJ/mol, confirming again the role of physical interactions in this adsorption process. Based on the positive value of ΔH^o, we prove the endothermic nature of TC adsorption. The positive value of ΔS^o reveals an increase in randomness at the interface of solid-solution over the process of adsorption, which implies some extent structural changes of TC molecule and surface of g-MoS_2-BC (Zhao et al., 2011).

3.7. Adsorption mechanisms

Based on the above analysis, we speculate that multiple mechanisms and various interactions including non-specific and specific binding are involved in the whole TC adsorption process onto g-MoS_2-BC, as illustrated in Fig. 7. According to the discussion in the influences of pH on TC adsorption (inhibiting effect in acid and alkali solution caused by electrostatic repulsion), it is confirmed that the electrostatic force actually do exist. To shed light on more mechanisms of TC adsorption, the FT-IR spectrum (Fig. 3c) experiments of g-MoS_2-BC and TC-loaded g-MoS_2-BC were conducted and analyzed further. Carboxyl (—COOH) plays an important role in making the surface negatively charged, which is ascribed to its ionization. Upon adsorption treatment, the C—O stretching vibration peak at 2860 cm^{-1} and C═O stretching peak at 1635 cm^{-1} are observed by slightly shifting to 2863 and

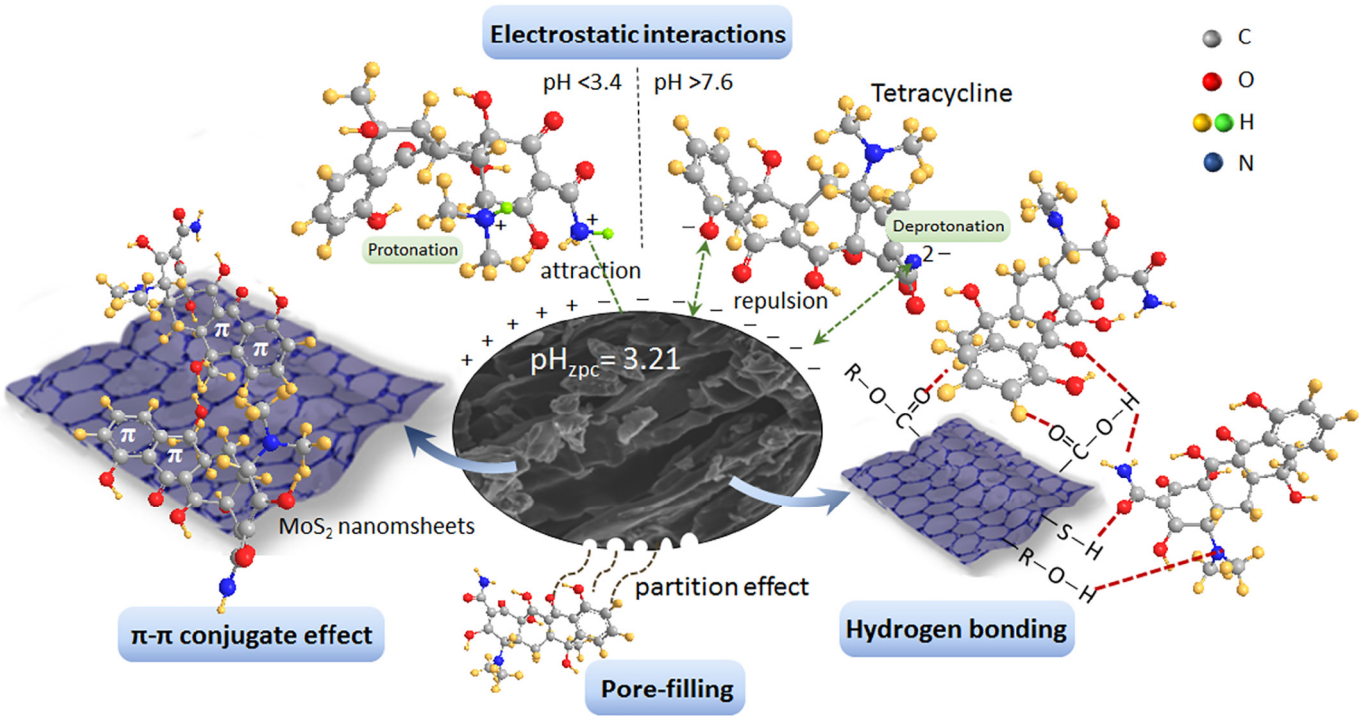

Fig. 7. The proposed mechanisms for the removal behavior of TC onto *g*-MoS_2-BC.

1637 cm^{-1}, respectively. These changes of peak position might be caused by the deprotonation of carboxyl, confirming the existence of electrostatic interaction between TC and *g*-MoS_2-BC in adsorption process. Moreover, the stretching vibration peaks at 2368, 1635, 1446, 1095 cm^{-1} derived from cumulated double bond, C═O, aromatic benzene ring skeleton, and C—O—C pyranose ring skeletal, respectively in composite occur in varying degrees of migration, which can be attributed to the π-π conjugate effect with benzene ring, double bonds, amino and other functional groups of TC molecule as π electron donator or acceptor. Considering the graphene-like layered structure of *g*-MoS_2 and the four aromatic rings in TC molecular structure, the mechanism of π-π stacking interaction between aromatic compound TC and π electron-rich regions of *g*-MoS_2-BC composite is proposed as a crucial one. Besides, the adsorption peaks at 667 cm^{-1} and around 3384–3450 cm^{-1} designated to S—H and O—H vibration, respectively shift to lower absorbance areas after adsorption experiment, manifesting the existence of hydrogen bond between TC and *g*-MoS_2-BC, it proves that hydrogen-bonding interaction is also one of the mechanisms affecting the TC adsorption process. Moreover, owing to the hydrophobic microenvironment of *g*-MoS_2-BC surface accommodating TC molecules, it shows promoting effect on the hydrogen bonding by the large π subunit of condensed aromatic structure (Zhang et al., 2016). Furthermore, the *g*-MoS_2-BC composite is considered as a tailor-made adsorbent for TC removal due to the appropriate pore-size distribution, since the increasing mesoporous might decrease the steric hindrance effect and enhance adsorption (Tang et al., 2018). By comparing the pore-size distribution of *g*-MoS_2-BC surface before and after TC adsorption (Fig. 3a), the mesoporous in the range of 2–20 nm was found to be significantly reduced undergone the adsorption, suggesting the pore-filling by partition effect is also one of the mechanisms that influencing the adsorption process.

3.8. Application on real water samples and its recyclability

River water and tap water were used as the medium of TC solution to study the practical application of *g*-MoS_2-BC in complex aqueous system. It can be observed from Fig. 5S, the adsorbed amount of TC by *g*-MoS_2-BC in river water and tap water are slightly higher than that in lab single system of deionized water. Because of the relatively low cationic concentration in the sampled water (Table 3S), the inhibitory effect is almost non-existent. The higher adsorption in the river water may be due to the wrapped and cross-linked of TC by the floccules or the additional adsorption by fine particles.

The recyclability of *g*-MoS_2-BC, an important indicator for assessing economy and applicability in large-scale application, was researched under three solution medium including deionized water, tap water and river water. It could be seen from Fig. 5S, regardless of the solution medium, the result describes a good recycle performance of *g*-MoS_2-BC with slight reduction after five cycles. After five adsorption/desorption cycles, the amount of adsorbed TC onto the recycled *g*-MoS_2-BC is about 163.07 mg/g in river water, which indicates the adsorbent still remains high adsorption capacity. Compared with other different adsorbents for TC adsorption (Table 4S), *g*-MoS_2-BC showed excellent performance in application and recyclability as well as the low-cost advantages, and it is considered as an adsorbent with great potential for removal of antibiotic contaminants from aquatic environment on a large scale application. Furthermore, the excellent catalytic ability of MoS_2 can be used to realize the regeneration of the saturated adsorbent by photo-degradation of loading TC molecules under light irradiation, which is worthy of further study because no solid-liquid separation is required.

4. Conclusions

The novel biochar-based nanocomposite had been prepared by a facile hydrothermal synthesis and showed a considerable adsorbed amount of TC with appropriate pore structure and abundant oxygen-containing functional groups. The hierarchical MoS_2 nanomaterials were proved to be embedded in the biochar, and the modification did improve the adsorption performance of materials. The results indicated that the adsorption of TC onto *g*-MoS_2-BC is a spontaneous and endothermic multilayer formation course that following three-step process, and it is strongly dependent on contact time, pH, temperature and initial concentration. The binding mechanisms, including electrostatic

interaction, pore-filling, hydrogen bonding, π-π interaction, and so on, are involved in the adsorption of TC molecules. Considering the cost-effective, high efficiency, excellent reusability and wide applicability, g-MoS_2-BC could be regard as a potential absorbent for removal the TC from polluted natural waters. Assembly of g-MoS_2 nanosheets onto biochar, a sustainable and reusable material, presents a wide range of possibilities for the further development of antibiotics-polluted water remediation without solid-liquid separation.

Acknowledgments

This research was financially supported by the National Natural Science Foundation of China (81773333, 51521006, 51479072, 51378190 and 51679082) and the Program for Changjiang Scholars and Innovative Research Team in University (IRT-13R17).

Appendix A. Supplementary data

Supplementary data to this article can be found online at https://doi.org/10.1016/j.scitotenv.2018.08.108.

References

Ahmed, M.B., Zhou, J.L., Ngo, H.H., Guo, W., Johir, M.A.H., Belhaj, D., 2017. Competitive sorption affinity of sulfonamides and chloramphenicol antibiotics toward functionalized biochar for water and wastewater treatment. Bioresour. Technol. 238, 306–312.

Berdinsky, A.S., Chadderton, L.T., Yoo, J.B., Gutakovsky, A.K., Fedorov, V.E., Mazalov, L.N., Fink, D., 2005. Structural changes of MoS2 nano-powder in dependence on the annealing temperature. Appl. Phys. A Mater. Sci. Process. 80 (1), 61–67.

Chang, K., Chen, W.X., 2011. L-Cysteine-assisted synthesis of layered MoS2/graphene composites with excellent electrochemical performances for lithium ion batteries. ACS Nano 5 (6), 4720–4728.

Chao, Y., Zhu, W., Wu, X., Hou, F., Xun, S., Wu, P., Ji, H., Xu, H., Li, H., 2014. Application of graphene-like layered molybdenum disulfide and its excellent adsorption behavior for doxycycline antibiotic. Chem. Eng. J. 243, 60–67.

Chao, Y., Yang, L., Ji, H., Zhu, W., Pang, J., Han, C., Li, H., 2017. Graphene-analogue molybdenum disulfide for adsorptive removal of tetracycline from aqueous solution: equilibrium, kinetic, and thermodynamic studies. Environ. Prog. Sustain. Energy 36 (3), 815–821.

Chen, M., Xu, P., Zeng, G.M., Yang, C.P., Huang, D.L., Zhang, J.C., 2015. Bioremediation of soils contaminated with polycyclic aromatic hydrocarbons, petroleum, pesticides, chlorophenols andheavymetalsby composting: applications, microbes and future research needs. Biotechnol. Adv. 33 (6), 745–755.

Cheng, M., Zeng, G.M., Huang, D.L., Lai, C., Xu, P., Zhang, C., Liu, Y., 2016. Hydroxyl radicals based advanced oxidation processes (AOPs) for remediation of soils contaminated with organic compounds: a review. Chem. Eng. J. 284, 582–598.

Deng, J.H., Zhang, X.R., Zeng, G.M., Gong, J.L., Niu, Q.Y., Liang, J., 2013. Simultaneous removal of Cd(II) and ionic dyes from aqueous solution using magnetic graphene oxide nanocomposite as an adsorbent. Chem. Eng. J. 226 (8), 189–200.

Gong, J.L., Wang, B., Zeng, G.M., Yang, C.P., Niu, C.G., Niu, Q.Y., Zhou, W.J., Liang, Y., 2009. Removal of cationic dyes from aqueous solution using magnetic multi-wall carbon nanotube nanocomposite as adsorbent. J. Hazard. Mater. 164 (2–3), 1517–1522.

Han, S., Liu, K., Hu, L., Teng, F., Yu, P., Zhu, Y., 2017. Superior adsorption and regenerable dye adsorbent based on flower-like molybdenum disulfide nanostructure. Sci. Rep. 7, 43599.

Homem, V., Santos, L., 2011. Degradation and removal methods of antibiotics from aqueous matrices—a review. J. Environ. Manag. 92 (10), 2304–2347.

Jahangiri-Rad, M., Nadafi, K., Mesdaghinia, A., Nabizadeh, R., Younesian, M., Rafiee, M., 2013. Sequential study on reactive blue 29 dye removal from aqueous solution by peroxy acid and single wall carbon nanotubes: experiment and theory. Iran. J Environ. Health Sci. Eng. 10 (1), 5.

Ji, L.L., Chen, W., Duan, L., Zhu, D.Q., 2009. Mechanisms for strong adsorption of tetracycline to carbon nanotubes: a comparative study using activated carbon and graphite as adsorbents. Environ. Sci. Technol. 43 (7), 2322–2327.

Kiran, V., Mukherjee, D., Jenjeti, R.N., Sampath, S., 2014. Active guests in the MoS2/MoSe2 host lattice: efficient hydrogen evolution using few-layer alloys of MoS2(1 − x)Se2x. Nanoscale 6 (21), 12856–12863.

Liang, J., Yang, Z., Tang, L., Zeng, G., Yu, M., Li, X., Wu, H., Qian, Y., Li, X., Luo, Y., 2017. Changes in heavy metal mobility and availability from contaminated wetland soil remediated with combined biochar-compost. Chemosphere 181, 281–288.

Liu, P.P., Wang, Q.R., Zheng, C.L., He, C., 2017a. Sorption of sulfadiazine, norfloxacin, metronidazole, and tetracycline by granular activated carbon: kinetics, mechanisms, and isotherms. Water Air Soil Pollut. 228 (4), 129.

Liu, S., Xu, W.H., Liu, Y.G., Tan, X.F., Zeng, G.M., Li, X., Liang, J., Zhou, Z., Yan, Z.L., Cai, X.X., 2017b. Facile synthesis of Cu(II) impregnated biochar with enhanced adsorption activity for the removal of doxycycline hydrochloride from water. Sci. Total Environ. 592, 546–553.

Long, F., Gong, J.L., Zeng, G.M., Chen, L., Wang, X.Y., Deng, J.H., Niu, Q.Y., Zhang, H.Y., Zhang, X.R., 2011. Removal of phosphate from aqueous solution by magnetic Fe–Zr binary oxide. Chem. Eng. J. 171 (2), 448–455.

Qiao, X.Q., Hu, F.C., Tian, F.Y., Hou, D.F., Li, D.S., 2016. Equilibrium and kinetic studies on MB adsorption by ultrathin 2D MoS2 nanosheets. RSC Adv. 6 (14), 11631–11636.

Qiao, X.Q., Zhang, Z.W., Tian, F.Y., Hou, D.F., Tian, Z.F., Li, D.S., Zhang, Q.C., 2017. Enhanced catalytic reduction of p-nitrophenol on ultrathin MoS2 nanosheets decorated with noble metal nanoparticles. Cryst. Growth Des. 17 (6), 3538–3547.

Ren, X.Y., Zeng, G.M., Tang, L., Wang, J.J., Wan, J., Liu, Y.N., Yu, J.F., Yi, H., Ye, S.J., Deng, R., 2018. Sorption, transport and biodegradation - an insight into bioavailability of persistent organic pollutants in soil. Sci. Total Environ. 610, 1154–1163.

Tan, X., Liu, Y., Zeng, G., Wang, X., Hu, X., Gu, Y., Yang, Z., 2015. Application of biochar for the removal of pollutants from aqueous solutions. Chemosphere 125, 70–85.

Tan, X., Liu, S., Liu, Y., Gu, Y., Zeng, G., Cai, X., Yan, Z., Yang, C., Hu, X., Chen, B., 2016a. One-pot synthesis of carbon supported calcined-Mg/Al layered double hydroxides for antibiotic removal by slow pyrolysis of biomass waste. Sci. Rep. 6, 39691.

Tan, X.F., Liu, Y.G., Gu, Y.L., Liu, S.B., Zeng, G.M., Cai, X., Hu, X.J., Wang, H., Liu, S.M., Jiang, L.H., 2016b. Biochar pyrolyzed from MgAl-layered double hydroxides pre-coated ramie biomass (*Boehmeria nivea* (L.) Gaud.): characterization and application for crystal violet removal. J. Environ. Manag. 184 (Pt 1), 85–93.

Tang, W.W., Zeng, G.M., Gong, J.L., Liang, J., Xu, P., Zhang, C., Huang, B.B., 2014. Impact of humic/fulvic acid on the removal of heavy metals from aqueous solutions using nanomaterials: a review. Sci. Total Environ. 468, 1014–1027.

Tang, L., Yu, J.F., Pang, Y., Zeng, G.M., Deng, Y.C., Wang, J.J., Ren, X.Y., Ye, S.J., Peng, B., Feng, H.P., 2018. Sustainable efficient adsorbent: alkali-acid modified magnetic biochar derived from sewage sludge for aqueous organic contaminant removal. Chem. Eng. J. 336, 160–169.

Theerthagiri, J., Senthil, R.A., Senthilkumar, B., Reddy Polu, A., Madhavan, J., Ashokkumar, M., 2017. Recent advances in MoS 2 nanostructured materials for energy and environmental applications – a review. J. Solid State Chem. 252, 43–71.

Tiwari, B., Sellamuthu, B., Ouarda, Y., Drogui, P., Tyagi, R.D., Buelna, G., 2017. Review on fate and mechanism of removal of pharmaceutical pollutants from wastewater using biological approach. Bioresour. Technol. 224, 1–12.

Vattikuti, S.V.P., Byon, C., 2016. Bi2S3 nanorods embedded with MoS2 nanosheets composite for photodegradation of phenol red under visible light irradiation. Superlattice. Microst. 100, 514–525.

Voiry, D., Salehi, M., Silva, R., Fujita, T., Chen, M.W., Asefa, T., Shenoy, V.B., Eda, G., Chhowalla, M., 2013. Conducting MoS2 nanosheets as catalysts for hydrogen evolution reaction. Nano Lett. 13 (12), 6222–6227.

Wan, J., Zeng, G., Huang, D., Hu, L., Xu, P., Huang, C., Deng, R., Xue, W., Lai, C., Zhou, C., Zheng, K., Ren, X., Gong, X., 2018. Rhamnolipid stabilized nano-chlorapatite: synthesis and enhancement effect on Pb-and Cd-immobilization in polluted sediment. J. Hazard. Mater. 343, 332–339.

Wang, H., Wen, F., Chen, Y., Sun, T., Meng, Y., Zhang, Y., 2016. Electrocatalytic determination of nitrite based on straw cellulose/molybdenum sulfide nanocomposite. Biosens. Bioelectron. 85, 692–697.

Wang, X., Wang, A., Ma, J., 2017. Visible-light-driven photocatalytic removal of antibiotics by newly designed C3N4@MnFe2O4-graphene nanocomposites. J. Hazard. Mater. 336, 81–92.

Wang, J., Yang, Q., Zhang, L., Liu, M., Hu, N., Zhang, W., Zhu, W., Wang, R., Suo, Y., Wang, J., 2018. A hybrid monolithic column based on layered double hydroxide-alginate hydrogel for selective solid phase extraction of lead ions in food and water samples. Food Chem. 257, 155–162.

Wu, Z., Zhong, H., Yuan, X., Wang, H., Wang, L., Chen, X., Zeng, G., Wu, Y., 2014. Adsorptive removal of methylene blue by rhamnolipid-functionalized graphene oxide from wastewater. Water Res. 2014 (67), 330–344.

Wu, H.P., Lai, C., Zeng, G.M., Liang, J., Chen, J., Xu, J.J., Dai, J., Li, X.D., Liu, J.F., Chen, M., Lu, L.H., Hu, L., Wan, J., 2017. The interactions of composting and biochar and their implications for soil amendment and pollution remediation: a review. Crit. Rev. Biotechnol. 37 (6), 754–764.

Xu, P., Zeng, G.M., Huang, D.L., Lai, C., Zhao, M.H., Wei, Z., Li, N.J., Huang, C., Xie, G.X., 2012a. Adsorption of Pb(II) by iron oxide nanoparticles immobilized Phanerochaete chrysosporium: equilibrium, kinetic, thermodynamic and mechanisms analysis. Chem. Eng. J. 203 (5), 423–431.

Xu, P., Zeng, G.M., Huang, D.L., Feng, C.L., Hu, S., Zhao, M.H., Lai, C., Wei, Z., Huang, C., Xie, G.X., Liu, Z.F., 2012b. Use of iron oxide nanomaterials in wastewater treatment: a review. Sci. Total Environ. 424, 1–10.

Yang, L., Zheng, X., Liu, M., Luo, S., Luo, Y., Li, G., 2017a. Fast photoelectro-reduction of CrVI over MoS2@TiO2 nanotubes on Ti wire. J. Hazard. Mater. 329, 230–240.

Yang, Q.F., Wang, J., Zhang, W.T., Liu, F.B., Yue, X.Y., Liu, Y.N., Yang, M., Li, Z.H., Wang, J.L., 2017b. Interface engineering of metal organic framework on graphene oxide with enhanced adsorption capacity for organophosphorus pesticide. Chem. Eng. J. 313, 19–26.

Yang, Q., Wang, Y., Wang, J., Liu, F., Hu, N., Pei, H., Yang, W., Li, Z., Suo, Y., Wang, J., 2018a. High effective adsorption/removal of illegal food dyes from contaminated aqueous solution by Zr-MOFs (UiO-67). Food Chem. 254, 241–248.

Yang, Q.F., Wang, J., Chen, X.Y., Yang, W.X., Pei, H.N., Hu, N., Li, Z.H., Suo, Y.R., Li, T., Wang, J.L., 2018b. The simultaneous detection and removal of organophosphorus pesticides by a novel Zr-MOF based smart adsorbent. J. Mater. Chem. A 6 (5), 2184–2192.

Ye, S., Zeng, G., Wu, H., Zhang, C., Dai, J., Liang, J., Yu, J., Ren, X., Yi, H., Cheng, M., Zhang, C., 2017a. Biological technologies for the remediation of co-contaminated soil. Crit. Rev. Biotechnol. 37 (8), 1062–1076.

Ye, S.J., Zeng, G.M., Wu, H.P., Zhang, C., Liang, J., Dai, J., Liu, Z.F., Xiong, W.P., Wan, J., Xu, P.A., Cheng, M., 2017b. Co-occurrence and interactions of pollutants, and their impacts on soil remediation-a review. Crit. Rev. Environ. Sci. Technol. 47 (16), 1528–1553.

Zeng, G., Wu, H., Liang, J., Guo, S., Hu, L., Xu, P., Liu, Y., Yuan, Y., He, X., He, Y., 2015. Efficiency of biochar and compost (or composting) combined amendments for reducing Cd, Cu, Zn and Pb bioavailability, mobility and ecological risk in wetland soil. RSC Adv. 5 (44), 34541–34548.

Zhang, M., Gao, B., Yao, Y., Xue, Y., Inyang, M., 2012. Synthesis, characterization, and environmental implications of graphene-coated biochar. Sci. Total Environ. 435–436, 567–572.

Zhang, Y., Zeng, G.M., Tang, L., Chen, J., Zhu, Y., He, X.X., He, Y., 2015. Electrochemical sensor based on electrodeposited graphene-Au modified electrode and nanoAu carrier amplified signal strategy for attomolar mercury detection. Anal. Chem. 87 (2), 989–996.

Zhang, C., Lai, C., Zeng, G., Huang, D., Yang, C., Wang, Y., Zhou, Y., Cheng, M., 2016. Efficacy of carbonaceous nanocomposites for sorbing ionizable antibiotic sulfamethazine from aqueous solution. Water Res. 95, 103–112.

Zhao, G.X., Li, J.X., Wang, X.K., 2011. Kinetic and thermodynamic study of 1-naphthol adsorption from aqueous solution to sulfonated graphene nanosheets. Chem. Eng. J. 173 (1), 185–190.

Zhao, Y., Zhang, X., Wang, C., Zhao, Y., Zhou, H., Li, J., Jin, H., 2017. The synthesis of hierarchical nanostructured MoS2/graphene composites with enhanced visible-light photo-degradation property. Appl. Surf. Sci. 412, 207–213.

Zhou, W.J., Hou, D.M., Sang, Y.H., Yao, S.H., Zhou, J., Li, G.Q., Li, L.G., Liu, H., Chen, S.W., 2014. MoO2 nanobelts@nitrogen self-doped MoS2 nanosheets as effective electrocatalysts for hydrogen evolution reaction. J. Mater. Chem. A 2 (29), 11358–11364.

Zhou, C.Y., Lai, C., Huang, D.L., Zeng, G.M., Zhang, C., Cheng, M., Hu, L., Wan, J., Xiong, W.P., Wen, M., Wen, X.F., Qin, L., 2018. Highly porous carbon nitride by supramolecular preassembly of monomers for photocatalytic removal of sulfamethazine under visible light driven. Appl. Catal. B Environ. 220, 202–210.

Zhu, C., Zhang, L., Jiang, B., Zheng, J., Hu, P., Li, S., Wu, M., Wu, W., 2016. Fabrication of Z-scheme Ag3PO4/MoS2 composites with enhanced photocatalytic activity and stability for organic pollutant degradation. Appl. Surf. Sci. 377, 99–108.